

Article

Open Access



Anion-rich Ir-doped CoO_x for boosting oxygen evolution reaction in water electrolysis

Wan Rong^{1,3}, Kang Huang^{2,*}, Longlong Dong³, Jiuyang Xia¹, Rui Dang³, Yunfei Chen³, Jianfei Liu³, Qigao Cao³, Bowei Zhang^{1,*}, Junsheng Wu^{1,*}

¹Institute of Advanced Materials and Technology, University of Science and Technology Beijing, Beijing 100083, China.

²School of Optical and Electronic Information & Jiangsu/Suzhou Key Laboratory of Biophotonics & International Joint Metacenter for Advanced Photonics and Electronics, Suzhou City University, Suzhou 215104, Jiangsu, China.

³Institute of Electronic Materials, Northwest Institute For Non-ferrous Metal Research, Xi'an 710016, Shaanxi, China.

***Correspondence to:** Prof. Kang Huang, School of Optical and Electronic Information & Jiangsu/Suzhou Key Laboratory of Biophotonics & International Joint Metacenter for Advanced Photonics and Electronics, Suzhou City University, No. 1188 Wuzhong Avenue, Suzhou 215104, Jiangsu, China. E-mail: huangkang@szcu.edu.cn; Prof. Bowei Zhang, Institute of Advanced Materials and Technology, University of Science and Technology Beijing, No. 30 Xueyuan Road, Beijing 100083, China. E-mail: bwzhang@ustb.edu.cn; Prof. Junsheng Wu, Institute of Advanced Materials and Technology, University of Science and Technology Beijing, No. 30 Xueyuan Road, Beijing 100083, China. E-mail: wujs@ustb.edu.cn

How to cite this article: Rong, W.; Huang, K.; Dong, L.; Xia, J.; Dang, R.; Chen, Y.; Liu, J.; Cao, Q.; Zhang, B.; Wu, J. Anion-rich Ir-doped CoO_x for boosting oxygen evolution reaction in water electrolysis. *Energy Mater.* **2025**, *5*, 500133. <https://dx.doi.org/10.20517/energymater.2025.21>

Received: 25 Jan 2025 **First Decision:** 18 Mar 2025 **Revised:** 14 Apr 2025 **Accepted:** 23 Apr 2025 **Published:** 9 Jul 2025

Academic Editor: Ho Won Jang **Copy Editor:** Fangling Lan **Production Editor:** Fangling Lan

Abstract

Owing to the sluggish kinetics of oxygen evolution reaction (OER) in electrochemical water electrolysis process, efficient and durable OER electrocatalysts are crucially needed. However, it is a great challenge to improve the comprehensive performance of OER electrocatalysts by utilizing various synergistic methodologies. To solve these issues, herein, Ir-doped Co-based compounds with regulated anions were synthesized using a coprecipitation method as the electrodes for boosting the OERs. Doping with Ir atoms modified the coordination environments and electronic structures of the $\text{CoO}_x\text{-CO}_3^{2-}$ lattice, and the generated Co^{3+} species promoted the generation of active species for the OER. It is worthwhile noting that a hybrid crystalline/amorphous $\text{IrCoO}_x\text{-CO}_3^{2-}$ compound was obtained with an Ir content of 10.09 wt.% and a large amount of Co^{3+} , and demonstrated excellent electrocatalytic OER performance. The overpotential required for the developed $\text{IrCoO}_x\text{-CO}_3^{2-}$ to achieve 10 mA cm^{-2} was as low as 207 mV with a very low Tafel slope of 61.7 mV dec^{-1} , which is better than the commercial IrO_2 . Furthermore, anions created in the IrCoO_x significantly promoted the OER, and their effects were decreased in the order of $\text{CO}_3^{2-} > \text{PO}_4^{3-} > \text{OH}^-$. This work clarifies the synergistic mechanism of cations and anions on the electrocatalytic OER performance of Co-based compounds, providing new insights for designs of high-performance OER



© The Author(s) 2025. **Open Access** This article is licensed under a Creative Commons Attribution 4.0 International License (<https://creativecommons.org/licenses/by/4.0/>), which permits unrestricted use, sharing, adaptation, distribution and reproduction in any medium or format, for any purpose, even commercially, as long as you give appropriate credit to the original author(s) and the source, provide a link to the Creative Commons license, and indicate if changes were made.



electrocatalysts for water electrolysis.

Keywords: Oxygen evolution reaction, Co-based compounds, Ir atoms, crystalline/amorphous structures, high-valence Co^{4+}

INTRODUCTION

Hydrogen as a green, sustainable, and stable renewable energy source has become the main focus for achieving the global goal of carbon neutrality. Currently water electrolysis using green electricity is a key development direction for the green hydrogen industry^[1-3]. However, oxygen evolution reaction (OER), one of the key processes that occur at the anode side of water electrolysis cells, involves a four-electron process with sluggish kinetics, severely affecting the successful applications of water electrolysis for hydrogen production^[4-6]. In the past decades, a number of OER electrocatalysts have been developed to increase the kinetics and chemical stability of electrodes in the electrolyte, and RuO_2 and IrO_2 are regarded as the two best OER electrocatalysts with comprehensive performance owing to their excellent electrocatalytic activity and stability^[7,8]. However, the rarity and high price of Ru and Ir severely prevent the widespread applications of these noble metal-based oxides for water electrolysis. Therefore, development of other high-performance and cost-effective OER electrocatalysts becomes a critical issue for improving the efficiency of the overall water electrolysis process.

Recently non-noble transition metal materials have been explored as OER electrocatalysts for industrial applications, mainly because of their low-cost and adjustable d-orbital electronic structure^[9,10]. Among those commonly reported electrocatalysts, Co-based compounds show remarkable electrocatalytic performance for the OER, which is mainly attributed to the variable valence states of Co ions^[11-14]. Compared with ions of other transition metal-based compounds with similar structures, Co^{3+} ions exhibit not only a good adsorption ability for reactants, but also high electrophilicity^[15-17]. However, the simple Co compounds often suffer from their unstable structures, poor conductivity, and low activity. Also the generation and conversion of different intermediates in the OER for these Co compounds hinder the low-cost green hydrogen production. To address these issues, extensive efforts are being made to enrich the active sites and improve conductivities of electrocatalysts by adding new components, modifying microstructures, adding defects, single atom engineering, and various functional modifications. Especially, doping noble metals into non-noble metal-based electrocatalysts has been considered as one of the most promising strategies for accelerating the OER recently. It is because this method not only allows for easy adjustment of the electronic state of electrocatalysts to stimulate active sites in the matrix, but also uses the doped noble metals as active sites^[18,19]. For example, doping one of the stable elements such as Ir into non-noble metal-based electrocatalysts results in excellent OER electrocatalytic performance^[20-28]. In addition to doping high-valence noble metals, adjusting the types of oxygen-containing anions is another favored method. For example, oxygen-containing anions such as carbonates and phosphates can accelerate the surface oxidation of Co-based compounds and much higher valence states can be achieved during the OER process^[29,30]. These modifications can enable Co-based compounds to form more Co^{3+} in the OER, which is beneficial for electrocatalytic performance. Therefore, simultaneous doping of Ir and oxygen-containing anions may lead to dramatic modifications in the electronic structures of Co-based compounds and improvements in their OER electrocatalytic performance.

In this study, coprecipitation - a simple, cost-effective, and easily scalable approach - was chosen to synthesize $\text{IrCoO}_x\text{-CO}_3^{2-}$, $\text{IrCoO}_x\text{-PO}_4^{3-}$, $\text{IrCoO}_x\text{-OH}^-$, and $\text{CoO}_x\text{-CO}_3^{2-}$ compounds with varying Ir doping contents and different anions. Among all the as-prepared compounds, we identified that the $\text{IrCoO}_x\text{-CO}_3^{2-}$

exhibited an excellent electrocatalytic activity for the OER in 1 M KOH electrolyte and an outstanding stability during continuous operation at 100 mA cm⁻² for 100 h. The IrCoO_x-CO₃²⁻ contained numerous well-dispersed Ir atoms and copious anionic carbonates stemming from the use of single nontoxic sodium carbonate as a precipitator, which increased the electron transfer efficiency for the OER. Both the Ir and Co served as active sites in the OER, and the Ir accelerated the generation of Co⁴⁺ active species. Such the synergistic effects of cations and anions on the deep reconstruction of Co-based OER electrocatalysts significantly enhance water electrolysis process.

EXPERIMENTAL

Materials

Cobalt nitrate hexahydrate [Co(NO₃)₂·6H₂O, AR], hydrogen hexachloroiridate (IV) hydrate (H₂IrCl₆·xH₂O, Ir ≥ 36%), sodium carbonate (Na₂CO₃, AR), sodium phosphate (Na₃PO₄, AR), sodium hydroxide (NaOH, AR) and Nafion® 117 (~5 wt%) were acquired from Aladdin; Potassium hydroxide (KOH, 95%) and iridium oxide (IrO₂, 99.9%) were acquired from Shanghai Macklin Biochemical Co., Ltd. Without additional processing, each chemical reagent was employed without further treatment.

Synthesis of various electrocatalysts

IrCoO_x-CO₃²⁻ was synthesized using a facile coprecipitation approach in the air. First, 1.455 g Co(NO₃)₂ (5 mmol) and 0.44 g H₂IrCl₆·xH₂O (0.8 mmol) were dissolved in 200 mL of water under vigorous stirring at 50 °C for 10 min. Meanwhile, 50 mL sodium carbonate fresh aqueous was introduced into above-mentioned solution slowly. After 4 h of reaction, a brown product was formed. The precipitate was centrifuged, washed five times with water and ethanol, and then vacuum-dried overnight at 60 °C. All the electrocatalysts doped with different Ir contents were synthesized using the same method, except with different amounts of H₂IrCl₆ precursor (e.g., 0.05, 0.1, 0.2, 0.4, and 1 mmol). Similarly, CoO_x-CO₃²⁻ was also synthesized with a similar method as IrCoO_x-CO₃²⁻, except that the H₂IrCl₆·xH₂O was not added as a precursor. IrCoO_x-PO₄³⁻ and IrCoO_x-OH⁻ were also synthesized with the same approach as above, except that sodium phosphate or sodium hydroxide was used to replace sodium carbonate, respectively.

Characterizations

Morphologies and structures were clarified using a scanning electron microscopy (SEM, Regulus 8230) and a transmission electron microscope (TEM, FEI Tecnai G2 F30). Element types and contents were analyzed using an energy dispersive spectrometry (EDS) equipped with the SEM and TEM. Images from a high-angle annular dark field-scanning transmission electron microscope (HAADF-STEM) were obtained using a JEOL STEM (ARM-200F). An X-ray diffractometer (Bruker D8 Advance) was utilized to test the X-ray diffraction (XRD) patterns of electrocatalysts. Fourier transmission infrared spectra (FT-IR) results were obtained using an FT-IR spectrometer (Thermo Nicolet IS 5). Raman spectra and *In-situ* Raman spectra were obtained using a Raman spectrometer (Horiba scientific-LabRAM HR). The valence states of the electrocatalysts were determined using an X-ray photoelectron spectrometer (ESCALAB 250, Al Kα source 1,486.68 eV).

Electrochemical measurements

The electrochemical tests were conducted using a CHI 760E electrochemical station with a three-electrode system, where the counter electrode and reference electrode in 1 M KOH electrolyte were a graphite and Hg/HgO/1 M KOH electrode, respectively. An acid-treated carbon cloth (1 cm × 1 cm) coated with the electrocatalysts was used as the working electrode. To prepare electrocatalyst dispersion, 10 mg electrocatalyst and 10 μL Nafion were dispersed in 1 ml water/ethanol (1:1 v/v) mixed solvent by sonication. Then 100 μL of such the dispersion was dripped onto the carbon cloth, making the electrocatalyst mass density was about 1 mg cm⁻². All the potentials obtained from electrochemical station were converted to be

referenced to hydrogen electrode (RHE) using $E_{\text{RHE}} = E_{\text{H}_2/\text{H}_2\text{O}} + 0.059 \times \text{pH} + 0.098 \text{ V}$ (25 °C). Linear sweep voltammetry (LSV) was conducted at a scan rate of 5 mV s⁻¹. Tafel slopes were calculated by plotting the overpotential vs. the logarithm of current density.

Electrochemical impedance spectroscopy (EIS) was conducted at the potential corresponding to 10 mA cm⁻² in a frequency range of 0.1–10⁵ Hz with an voltage perturbation of 5 mV in amplitude. The stability was assessed by conducting chronopotentiometry on carbon cloth loaded with the electrocatalysts, while maintaining at 10 mA cm⁻² for the OER. The double layer capacitance (C_{dl}) measurement was conducted using cyclic voltammetry (CV) curves with different scan rates (10–50 mV s⁻¹) in 0.924–0.974 V vs. RHE. Electrochemical surface area (ECSA) can be calculated by $\text{ECSA} = (C_{\text{dl}} / C_s) \times S$. The value of C_s was estimated as 40 μF cm⁻² in this study. The turnover frequency (TOF) values were recorded under the assumption that all metal ions exhibited electrocatalytic activity.

Computational methods

The first-principle calculations were carried out using density functional theory (DFT), implemented in the Vienna Ab Initio Simulation Package (VASP) code. The frozen-core projector augmented-wave (PAW) method was used to describe the interaction between the atomic cores and the valence electron density. The exchange-correlation potential was approximated within the generalized gradient approximation (GGA)^[31,32]. The dispersion-corrected DFT-D3 schemes were employed to describe the Van der Waals (vdW) interactions, and Plane-wave cutoff energy was set to 450 eV^[33,34]. The Brillouin zone in reciprocal space was sampled with a Γ -centered Monkhorst-Pack scheme and gamma-point grids for geometry optimization and electronic structure calculations. The computational hydrogen electrode (CHE) model was used to calculate the change in Gibbs free energy (ΔG).

RESULTS AND DISCUSSION

The morphology of IrCoO_x-CO₃²⁻ was characterized using a scanning electron microscope (SEM). It exhibits the characteristic morphology of nanoparticles (diameter: ~20 nm) [Figure 1A]. The structure of IrCoO_x-CO₃²⁻ was further analyzed using TEM. Figure 1B shows the high magnification TEM image of IrCoO_x-CO₃²⁻, which is consistent with SEM image. A series of bright diffraction rings in the selected area electron diffraction (SAED) image [Figure 1C] confirmed the polycrystalline structure of IrCoO_x-CO₃²⁻. Figure 1D shows the high-resolution TEM (HRTEM) image of IrCoO_x-CO₃²⁻. For further structural analysis, four different nanoparticles [designated as 1, 2, 3, and 4 shown in Figure 1D] were selected. Figure 1E shows the high-resolution lattice image of nanoparticle 1 in Figure 1D. The lattice spacings of 0.24 and 0.20 nm are indexed to the (3 1 1) and (4 0 0) facets of Co₃O₄, respectively. Figure 1F shows the lattice image of nanoparticle 2 in Figure 1D. The lattice spacing of 0.21 nm can be indexed to the (4 0 0) facet of Co₃O₄. However, the lattice image [Figure 1G] of nanoparticle 3 in Figure 1D is quite different from those of nanoparticles 1 and 2. It displays severely distorted and randomly distributed lattice patterns, suggesting the formation of amorphous structure. The weak diffraction rings in fast Fourier transformation (FFT) pattern [inset image in Figure 1G] also prove the formation of amorphous structure. Figure 1H shows the lattice image of nanoparticle 4 in Figure 1D, revealing the formation of defects (i.e., dislocations at the interface between crystalline and amorphous regions). Based on the HRTEM results, we can confirm that the hybrid crystalline/amorphous structures have been generated. Previous studies reported that amorphous structures are beneficial for enhancing the electrocatalytic OER performance, whereas crystalline structures are conducive to the stability of the system, and synergistic effects of these two different crystalline structures could achieve both improved activity and stability^[35,36]. Moreover, such hybrid crystalline/amorphous structures could form highly mismatched interfaces between the crystalline and amorphous regions, which effectively promoted the formation of OER active sites^[37–39]. The HAADF-STEM images

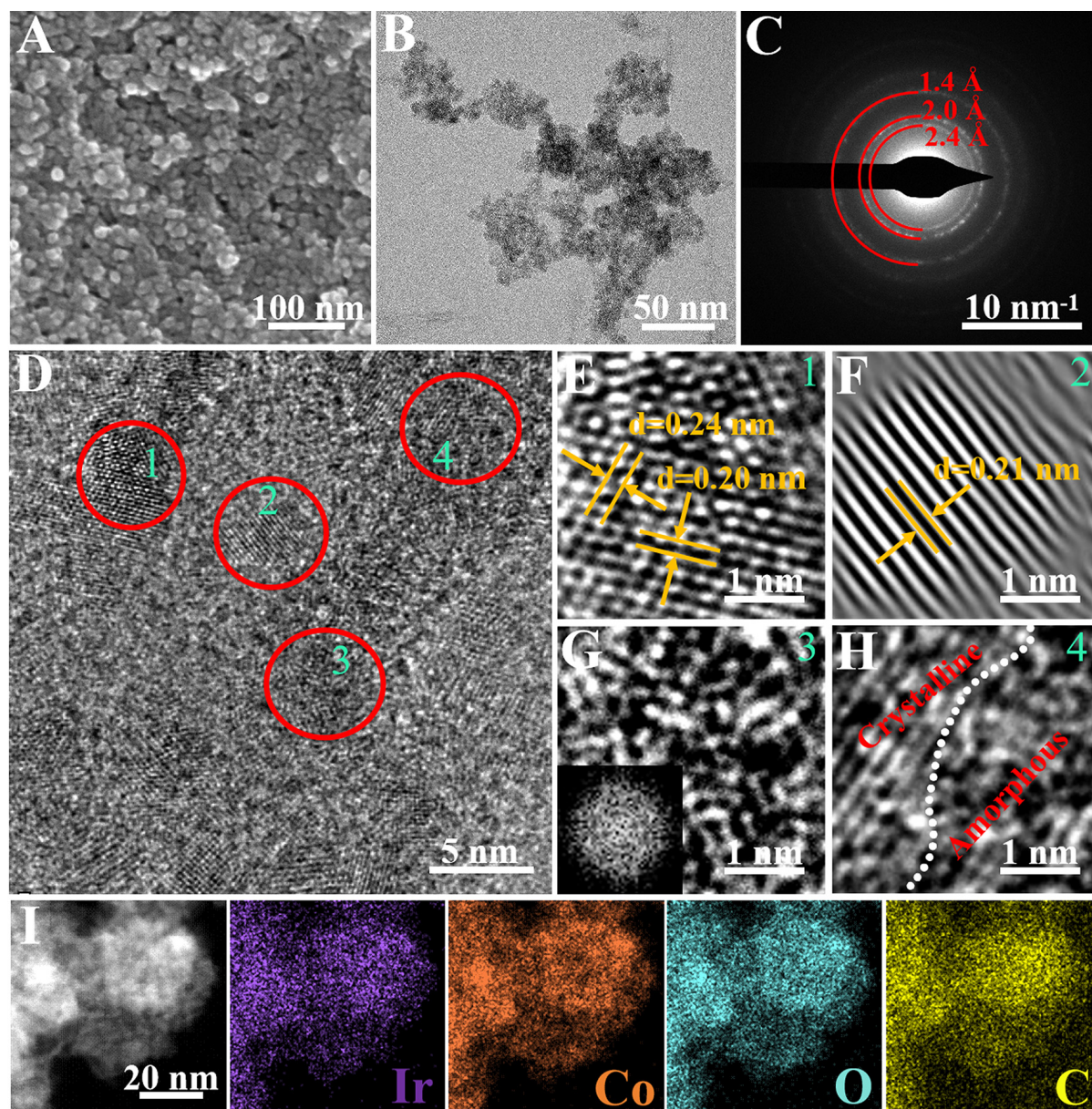


Figure 1. Morphology and structure characterizations of $\text{IrCoO}_x\text{-CO}_3^{2-}$. (A) SEM image, (B) TEM image, (C) SAED pattern, (D) HRTEM image, (E) Atomic lattice image of nanoparticle 1 in (D), (F) Atomic lattice image of nanoparticle 2 in (D), (G) Atomic lattice image of nanoparticle 3 in (D) (inset image: FFT pattern), (H) Atomic lattice image of nanoparticle 4 in (D), (I) HAADF image and elemental mappings.

[Supplementary Figure 1] exhibit many bright spots corresponding to those of the Ir atoms, which were uniformly distributed inside the nanoparticles. The dispersion state of each element was further analyzed using the EDS elemental mapping. As shown in Figure 1I, all the elements are uniformly distributed in the nanoparticles. For comparisons, $\text{CoO}_x\text{-CO}_3^{2-}$ without Ir doping and IrCoO_x modified with other anions (PO_4^{3-} and OH^-) were synthesized using the same process. Given that the synthetic protocol involved solely modifying the type of precipitant, all the as-prepared IrCoO_x demonstrate approximate Ir content (~ 11 wt.%) as quantified by inductively coupled plasma optical emission spectrometry (ICP-OES) analysis [Supplementary Table 1]. The morphologies and structures of them were also analyzed using SEM and TEM [Supplementary Figures 2-4]. Except for $\text{CoO}_x\text{-CO}_3^{2-}$ exhibiting two-dimensional nanosheet

morphology (thickness: ~ 20 nm), all other as-synthesized electrocatalysts are characterized as nanoparticles (diameter: ~ 20 nm). Despite differences in morphology, SAED/HRTEM analysis reveals that all the as-synthesized electrocatalysts possess hybrid crystalline/amorphous structures and uniform composition. The nanoscale size can enable electrocatalysts to have a higher surface area, especially $\text{IrCoO}_x\text{-CO}_3^{2-}$ ($101.71 \text{ m}^2 \text{ g}^{-1}$) [Supplementary Figure 5]. In addition, a series of $\text{IrCoO}_x\text{-CO}_3^{2-}$ with various Ir content were also synthesized to investigate the doping-dependent electrocatalytic OER performance [Supplementary Figure 6, Supplementary Table 2].

The XRD results are shown in Figure 2A, Supplementary Figures 7 and 8. The crystalline phase of $\text{CoO}_x\text{-CO}_3^{2-}$ was identified as basic cobalt carbonate (JCPD No.48-0083), which exhibited poor crystallinity. Meanwhile, the major XRD diffraction peaks of $\text{IrCoO}_x\text{-CO}_3^{2-}$ were found to shift toward the diffraction peaks of Co_3O_4 (JCPD No.42-1467), whereas its crystallinity remained very poor [Figure 2A]. This indicates that Ir doping can induce a phase transformation in $\text{CoO}_x\text{-CO}_3^{2-}$. The Raman spectra shown in Figure 2B reveal the element bonding states and chemical coordination environment of the electrocatalysts. The spectrum of $\text{CoO}_x\text{-CO}_3^{2-}$ displays a strong peak at 521 cm^{-1} corresponding to the vibration mode of Co-O, and two other strong peaks at $1,150$ and $1,530 \text{ cm}^{-1}$ corresponding to carbonates^[40-42]. After doping Ir, the peaks corresponding to carbonates disappeared. Meanwhile, $\text{IrCoO}_x\text{-CO}_3^{2-}$ displays new peaks at 480 and 664 cm^{-1} , which are attributed to the bending vibration modes of Co-O in Co_3O_4 , and another mode at 598 cm^{-1} which is assigned to that of CoOOH ^[43]. FT-IR spectra [Figure 2C] are used to identify the functional groups formed on electrocatalysts. The broad bands at $3,440 \text{ cm}^{-1}$ in all the samples are attributed to the stretching and bending vibration modes of hydroxyl groups in water molecules^[44]. The two intense bands at 575 and 660 cm^{-1} in all the spectra are consistent with those induced by the Co-O stretching vibration (i.e., 568 and 664 cm^{-1})^[45]. In addition, the C-O intense bands at approximately $1,490$ and 810 cm^{-1} are attributed to CO_3^{2-} ^[44,46]. All these results indicate that the Ir doping successfully modified the structure of $\text{CoO}_x\text{-CO}_3^{2-}$.

A strong synergistic effect among various elements in the electrocatalysts is vital for the electrocatalytic performance. Electronic structures of $\text{CoO}_x\text{-CO}_3^{2-}$ and $\text{IrCoO}_x\text{-CO}_3^{2-}$ were characterized using X-ray photoelectron spectroscopy (XPS). The full survey XPS spectra of $\text{CoO}_x\text{-CO}_3^{2-}$ and $\text{IrCoO}_x\text{-CO}_3^{2-}$ reveal the presence of Co, O, C on $\text{CoO}_x\text{-CO}_3^{2-}$ and Ir, Co, O, C on $\text{IrCoO}_x\text{-CO}_3^{2-}$, respectively [Supplementary Figure 9]. The Ir 4f XPS spectrum of $\text{IrCoO}_x\text{-CO}_3^{2-}$ showed the presence of Ir^{3+} and Ir^{4+} , whereas only Ir^{4+} was detected on IrO_2 [Figure 2D]^[33]. To understand Ir doping effect on the valence state of Co, the Co 2p spectra [Figure 2E] of $\text{CoO}_x\text{-CO}_3^{2-}$ and $\text{IrCoO}_x\text{-CO}_3^{2-}$ were compared. The two peaks of Co $2p^{3/2}$ at 780.2 eV and Co $2p^{1/2}$ at 796.3 eV are associated with Co^{3+} , and the two peaks of Co $2p^{3/2}$ at 782.9 eV and Co $2p^{1/2}$ at 798.5 eV are associated with Co^{2+} ^[14,33]. Co^{3+} also appeared on the surface of $\text{CoO}_x\text{-CO}_3^{2-}$, which can be attributed to the oxidation of Co^{2+} . The $\text{Co}^{3+}/\text{Co}^{2+}$ ratio on $\text{CoO}_x\text{-CO}_3^{2-}$ was ~ 0.64 . After Ir doping, the proportion of Co^{3+} on $\text{IrCoO}_x\text{-CO}_3^{2-}$ was increased substantially and the $\text{Co}^{3+}/\text{Co}^{2+}$ ratio reached ~ 1.71 . This suggested the occurrence of an electron transfer from Co^{2+} to Ir^{4+} in $\text{IrCoO}_x\text{-CO}_3^{2-}$. When Ir^{4+} was partially converted into Ir^{3+} by accepting electrons from Co^{2+} , the latter was converted into Co^{3+} . This can be attributed to the higher electronegativity of Ir (2.20) than that of Co (1.88) according to the Pauling electronegativity scale. Moreover, the increased $\text{Co}^{3+}/\text{Co}^{2+}$ ratio after Ir doping increased the O content, possibly forming Ir-O-Co pairs which could be served as a bridge for the electron transfer between Ir and Co. The internal electron transfer promoted the massive formation of Co^{3+} , as indicated by the apparent shift of the XRD diffraction peaks of $\text{IrCoO}_x\text{-CO}_3^{2-}$ toward those of Co_3O_4 [Figure 2A]. Owing to the stronger covalency of doped high-valence Ir, the O 1s XPS spectrum of $\text{IrCoO}_x\text{-CO}_3^{2-}$ displayed more lattice O (M-O) than that of $\text{CoO}_x\text{-CO}_3^{2-}$ [Figure 2F]^[47,48]. The high-valence Co formed on $\text{IrCoO}_x\text{-CO}_3^{2-}$ was likely to bind with lattice O. Meanwhile, the high-valence Co and lattice O can not only enhance the adsorption of

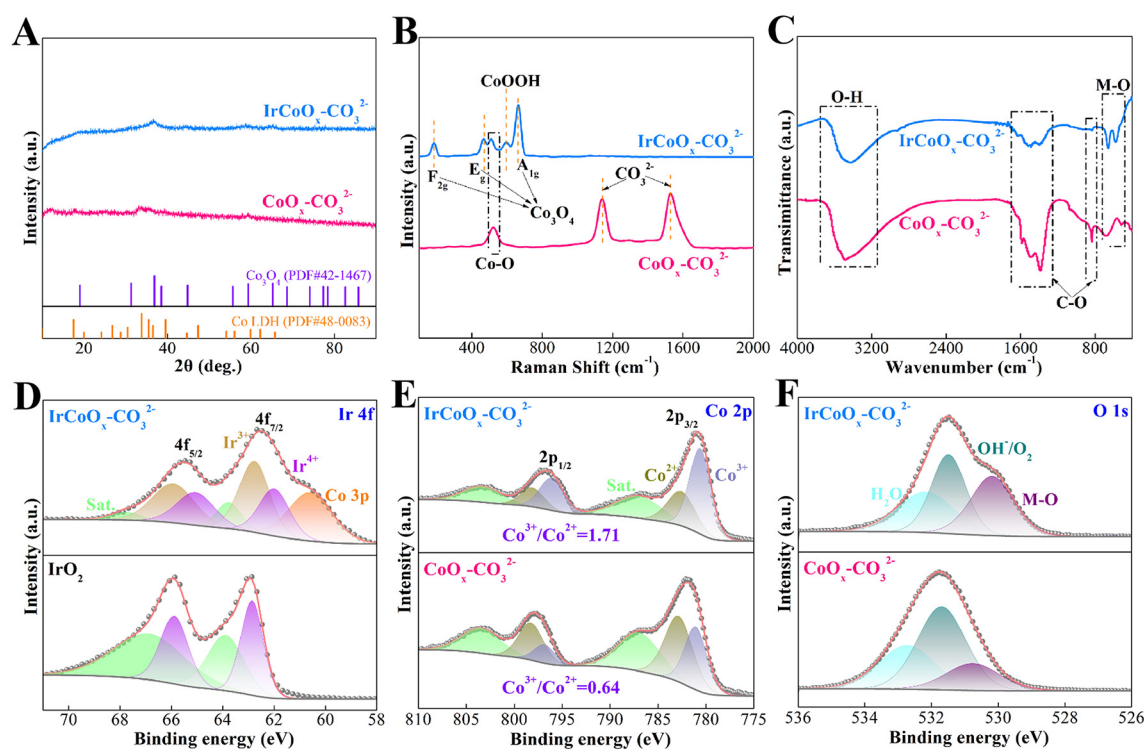


Figure 2. (A) XRD patterns, (B) Raman and (C) FT-IR spectra of $\text{CoO}_x\text{-CO}_3^{2-}$ and $\text{IrCoO}_x\text{-CO}_3^{2-}$. (D) Ir 4f XPS spectra of IrO_2 and $\text{IrCoO}_x\text{-CO}_3^{2-}$. (E) Co 2p, and (F) O 1s XPS spectra of $\text{CoO}_x\text{-CO}_3^{2-}$ and $\text{IrCoO}_x\text{-CO}_3^{2-}$.

OER intermediates (*OH and *OOH), but can also promote the rapid formation of active species on the surface of electrocatalyst during the OER process^[49,50]. For comparisons, the XPS spectra [Supplementary Figures 10 and 11] of $\text{IrCoO}_x\text{-PO}_4^{3-}$ and $\text{IrCoO}_x\text{-OH}^-$ were also obtained. The mixed-valence states of metal elements on $\text{IrCoO}_x\text{-PO}_4^{3-}$ and $\text{IrCoO}_x\text{-OH}^-$ were similar to that on $\text{IrCoO}_x\text{-CO}_3^{2-}$, but the content of high-valence Co has decreased.

The electrocatalytic OER performance of the as-prepared electrocatalysts and commercial IrO_2 was tested in 1 M KOH. As shown in Figure 3A, the $\text{IrCoO}_x\text{-CO}_3^{2-}$ exhibited outstanding OER activity over others. The $\text{IrCoO}_x\text{-CO}_3^{2-}$ delivered a current density of 10 mA cm^{-2} with an overpotential (η_{10}) of only 207 mV, whereas the η_{10} values of $\text{IrCoO}_x\text{-PO}_4^{3-}$, $\text{IrCoO}_x\text{-OH}^-$, CoO-CO_3^{2-} and commercial IrO_2 were 219, 241, 316, and 372 mV, respectively [Figure 3B]. Notably, Ir doping demonstrates superior efficacy over anionic modification in boosting electrocatalytic OER activity, where the optimal Ir content (10.09 wt.%) results in a low overpotential of 207 mV at 10 mA cm^{-2} [Supplementary Figures 12 and 13]. The excellent electrocatalytic OER activity for $\text{IrCoO}_x\text{-CO}_3^{2-}$ is mainly attributed to the rapid activation, caused by the lower initial potential and fewer times in CV activation [Supplementary Figure 14]. The Tafel slope was also used to verify the electron transfer rate of electrocatalyst in the OER. The Tafel slope of $\text{IrCoO}_x\text{-CO}_3^{2-}$ (61.7 mV dec^{-1}) is lower than those of $\text{IrCoO}_x\text{-PO}_4^{3-}$ (64.9 mV dec^{-1}), $\text{IrCoO}_x\text{-OH}^-$ (68.1 mV dec^{-1}), $\text{CoO}_x\text{-CO}_3^{2-}$ (74.8 mV dec^{-1}), and commercial IrO_2 ($141.7 \text{ mV dec}^{-1}$), revealing that the $\text{IrCoO}_x\text{-CO}_3^{2-}$ was more favorable for the OER under the alkaline conditions [Figure 3C]. To elucidate the differences in kinetics, EIS [Figure 3D] was employed to examine the charge transfer capabilities of the electrocatalysts in the OER. Supplementary Figure 15 shows the equivalent circuit which was used to analyze the processes of two different electrochemical reactions occurring on working electrodes. Among the as-synthesized electrocatalysts, the $\text{IrCoO}_x\text{-CO}_3^{2-}$ exhibited the lowest charge transfer resistance (R_{ct}) of 2.35Ω , and those of

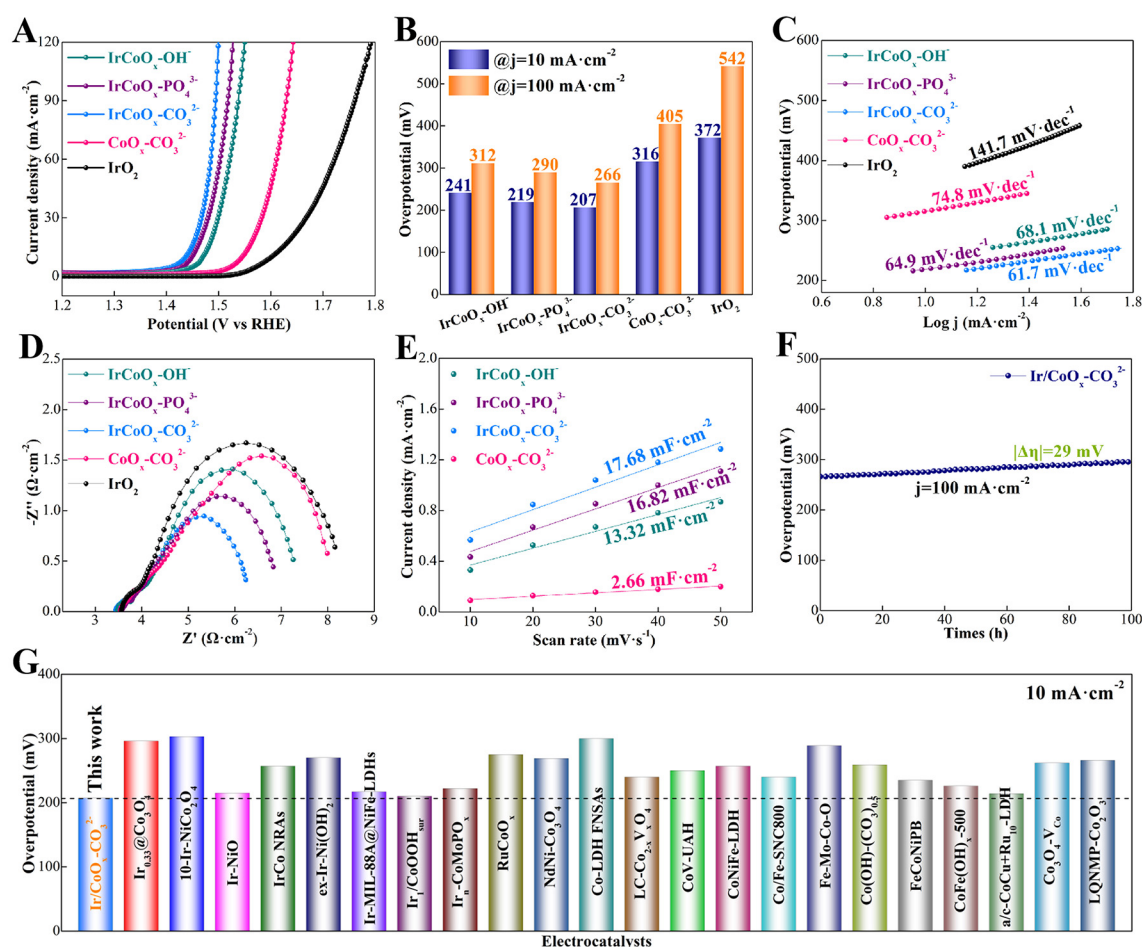


Figure 3. Electrocatalytic OER performance of various electrocatalysts in 1 M KOH. (A) LSV curves, (B) Overpotentials at the current densities of 10 and 100 mA cm⁻², (C) Tafel slopes, (D) EIS spectra and (E) C_{dl} values of CoO_x-CO₃²⁻, IrCoO_x-CO₃²⁻, IrCoO_x-PO₄³⁻, IrCoO_x-OH⁻, respectively. (F) OER stability testing of IrCoO_x-CO₃²⁻ at 100 mA cm⁻²; (G) A comprehensive comparison of overpotentials at 10 mA cm⁻² for IrCoO_x-CO₃²⁻ electrode with reported state-of-the-art Ir doped or Co-based electrocatalysts.

IrCoO_x-PO₄³⁻ (2.82 Ω), IrCoO_x-OH⁻ (3.16 Ω), and CoO_x-CO₃²⁻ (3.4 Ω) were also lower than that of commercial IrO₂ (3.9 Ω). [Supplementary Table 3](#) summarizes all the obtained data, which reveals that Ir and carbonates caused considerably decreased R_{ct} values of the electrocatalysts. Intrinsic OER activities of the as-synthesized electrocatalysts were further assessed by determining the C_{dl} from CV curves [[Supplementary Figure 16](#)], which showed a linear relationship with the ECSA. [Figure 3E](#) shows that the C_{dl} value of IrCoO_x-CO₃²⁻ was 17.68 mF cm⁻², which was higher than those of IrCoO_x-PO₄³⁻ (16.82 mF cm⁻²), IrCoO_x-OH⁻ (13.32 mF cm⁻²), and CoO_x-CO₃²⁻ (2.66 mF cm⁻²). This indicates that Ir doping and the intercalation of carbonate promoted the generation of abundant active sites for the OER [[Supplementary Figure 17](#)]. Furthermore, the TOF value of IrCoO_x-CO₃²⁻ at a potential of 1.49 V vs. RHE (η = 260 mV) was measured and the reading is 0.01871 s⁻¹ [[Supplementary Figure 18](#), [Supplementary Table 4](#)]. This reading is considerably higher than those of IrCoO_x-PO₄³⁻ (0.00947 s⁻¹), IrCoO_x-OH⁻ (0.00536 s⁻¹), CoO_x-CO₃²⁻ (0.00054 s⁻¹), and commercial IrO₂ (0.00011 s⁻¹), indicating that IrCoO_x-CO₃²⁻ exhibits the highest instantaneous efficiency for the OER. Stability is also an extremely important indicator for evaluating the OER performance of electrocatalysts, in addition to activity. To explore the stability of IrCoO_x-CO₃²⁻ for the OER, the chronopotentiometry (V-t) curve [[Figure 3F](#)] tested at 10 mA cm⁻² was obtained. The overpotential for the OER of IrCoO_x-CO₃²⁻ was increased only by 29 mV

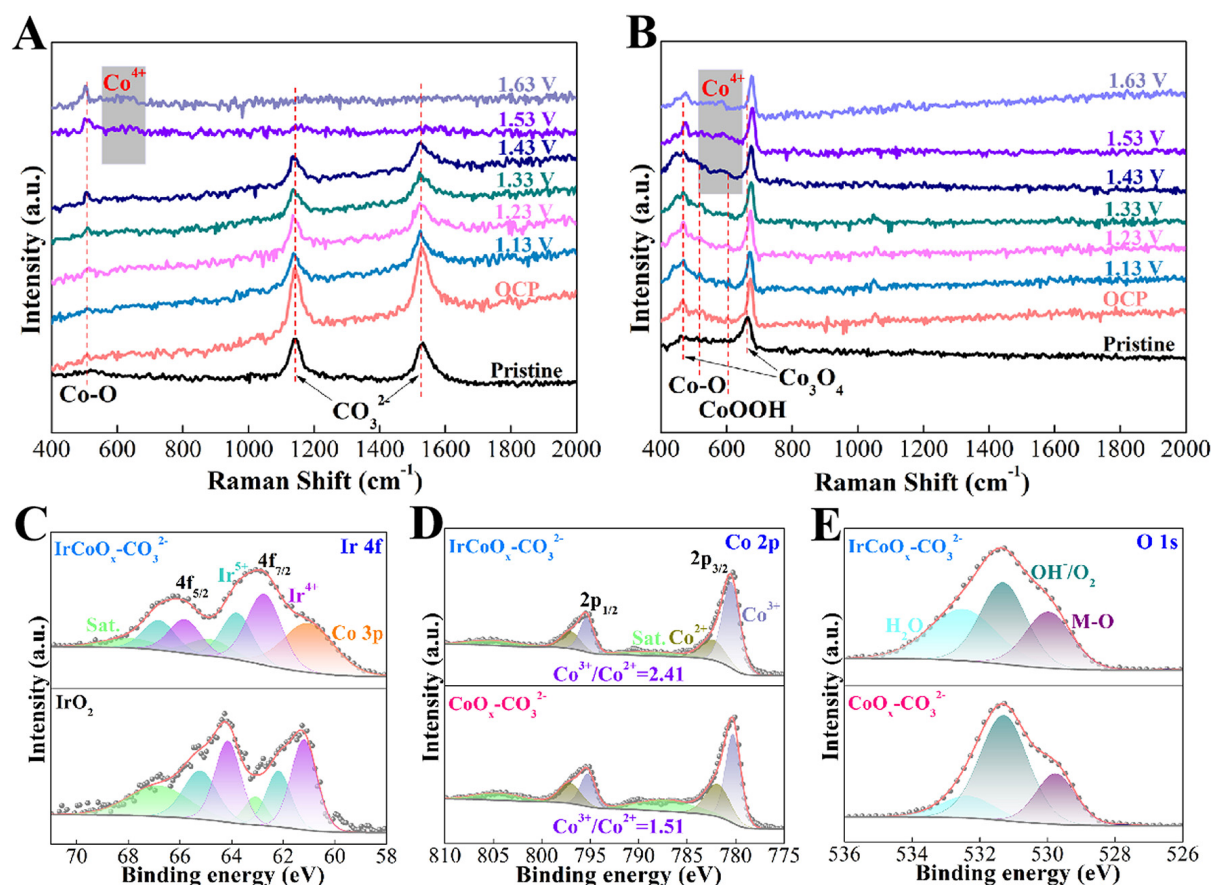


Figure 4. *In situ* Raman spectra of the species formed in the OER electrocatalyzed by (A) $\text{CoO}_x\text{-CO}_3^{2-}$ and (B) $\text{IrCoO}_x\text{-CO}_3^{2-}$. (C) Ir 4f XPS spectra of IrO_2 and $\text{IrCoO}_x\text{-CO}_3^{2-}$ after the OER stability testing, (D) Co 2p, and (E) O 1s XPS spectra of $\text{CoO}_x\text{-CO}_3^{2-}$ and $\text{IrCoO}_x\text{-CO}_3^{2-}$ after the OER stability testing.

after being maintained for 100 h at 100 mA cm^{-2} , indicating that $\text{IrCoO}_x\text{-CO}_3^{2-}$ has excellent electrocatalytic OER stability. Remarkably, the electrocatalytic OER performance of $\text{IrCoO}_x\text{-CO}_3^{2-}$ outperforms most of reported state-of-the-art Ir-doped or Co-based electrocatalysts for alkaline OER [Figure 3G, Supplementary Table 5].

All electrochemical results indicated that the Ir doping had a more significant impact on the electrocatalytic OER performance of Co-based compounds compared to the influence of different anions (CO_3^{2-} , PO_4^{3-} , OH^-). To further investigate the real OER active species of the $\text{CoO}_x\text{-CO}_3^{2-}$ and $\text{IrCoO}_x\text{-CO}_3^{2-}$ during the OER process, *in situ* Raman spectroscopy was performed to monitor the dynamic process. Figure 4A shows the obtained Raman spectra of the $\text{CoO}_x\text{-CO}_3^{2-}$ electrode during the OER process. Since the peaks of carbonates were very strong, those of Co-O at 521 cm^{-1} appeared relatively weak. With the increase of the applied potential, the peak of Co-O became more noticeable. When the potential was increased to 1.53 V, the corresponding peaks of carbonate ($1,150$ and $1,530 \text{ cm}^{-1}$) became vanished and a new peak of Co^{4+} emerged at 589 cm^{-1} . This clearly demonstrates that Co^{2+} or Co^{3+} in $\text{CoO}_x\text{-CO}_3^{2-}$ was transformed into Co^{4+} after the potential reached a certain value^[51,52]. For comparisons, we have obtained the *in situ* Raman spectra of the $\text{IrCoO}_x\text{-CO}_3^{2-}$ electrode during the OER process, and the obtained data are shown in Figure 4B. With increasing applied potential, the corresponding peaks of Co_3O_4 shifted to higher wavenumbers. A new peak emerged at 589 cm^{-1} when the potential was increased to 1.43 V, and this corresponds to the conversion from Co^{2+} or Co^{3+} to Co^{4+} due to the formation of high-valence cobalt oxide active species^[51-53]. These *in situ*

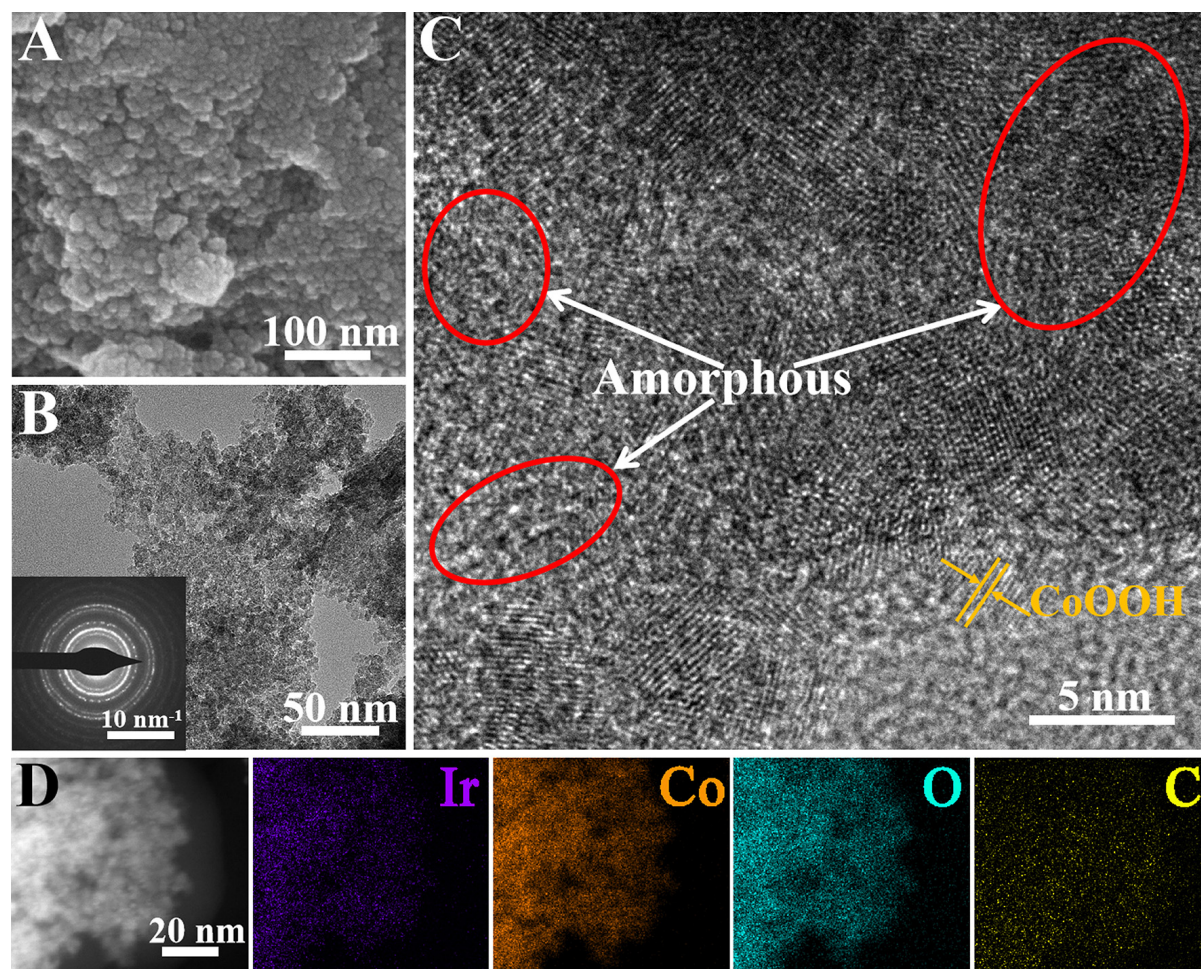


Figure 5. Morphology and structure characterizations of $\text{IrCoO}_x\text{-CO}_3^{2-}$ after the OER stability testing. (A) SEM image, (B) TEM image (Inset image: Corresponding SAED pattern), (C) HRTEM image, (D) HAADF image and elemental mappings.

Raman spectra of $\text{CoO}_x\text{-CO}_3^{2-}$ and $\text{IrCoO}_x\text{-CO}_3^{2-}$ during the OER process showed that the potential required to form Co^{4+} on the surface of $\text{IrCoO}_x\text{-CO}_3^{2-}$ was 100 mV lower than that of $\text{CoO}_x\text{-CO}_3^{2-}$. This can be due to Co^{3+} being more conducive to the formation of high-valence Co^{4+} , while there was more Co^{3+} in $\text{IrCoO}_x\text{-CO}_3^{2-}$ than in $\text{CoO}_x\text{-CO}_3^{2-}$ according to XPS results [Figure 2E].

The electronic structure of $\text{IrCoO}_x\text{-CO}_3^{2-}$ was further studied using XPS after the OER stability testing. As shown in Supplementary Figure 19, the main elements on $\text{CoO}_x\text{-CO}_3^{2-}$ were Co, O, C, and F, and those on $\text{IrCoO}_x\text{-CO}_3^{2-}$ after the OER were Ir, Co, O, C, and F^[54]. The F element came from the remaining Nafion solution. The Ir 4f XPS spectra [Figure 4C] showed that the Ir on $\text{IrCoO}_x\text{-CO}_3^{2-}$ was in a high-valence state (+5 valence), as was also the case for IrO_2 ^[33]. The Co 2p XPS spectra [Figure 4D] showed that the $\text{Co}^{3+}/\text{Co}^{2+}$ ratios on $\text{IrCoO}_x\text{-CO}_3^{2-}$ were increased to 2.41, respectively. The transition of Ir and Co to higher valence states revealed that $\text{IrCoO}_x\text{-CO}_3^{2-}$ experienced an irreversible oxidation process in the OER. Importantly, the presence of high-valence Ir in the OER can promote the conversion of Co^{2+} to Co^{3+} due to the continuous interaction between Ir and Co. Meanwhile, the higher valence state of Ir also demonstrated that the doped Ir atoms are effective active sites to accelerate the OER in conjunction with the Co-active sites. The O 1s XPS spectra [Figure 4E] showed that $\text{IrCoO}_x\text{-CO}_3^{2-}$ exhibited more lattice O (M-O) after the OER, which can be attributed to the formation of high-valence active species. Since the M-O bonds formed by high-valence

metal ions and O had lower energy in the oxidation-reduction process, the presence of abundant high-valence Ir can strengthen the binding between Co ions and O^[47,55]. In addition, the DFT calculation results were used to further determine the roles of Ir and Co in OER. As shown in [Supplementary Figure 20](#), the rate-determining steps of Co and Ir sites on the surface of IrCoO_x-CO₃²⁻ are all associated with the generation of O*. There is a lower free energy (1.57 eV) on the Co sites than that (1.87 eV) on the Ir sites, indicating that the Co sites are the main active centers for the OER. Compared to Ir sites on IrCoO_x-CO₃²⁻, those on the IrO₂ (110) with the same rate-determining step exhibit much higher free energy (e.g., 2.29 eV). This implies that the Ir sites on IrCoO_x-CO₃²⁻ are the second most active sites after Co. Therefore, the coordinated roles of Ir and Co in the OER promoted the formation of M-O bonds on IrCoO_x-CO₃²⁻.

The structure and composition stability of electrocatalysts are all the key factors for ensuring their long-term usage. Hence, IrCoO_x-CO₃²⁻ was characterized via SEM and TEM after the OER stability testing. As shown in [Figure 5A](#), the IrCoO_x-CO₃²⁻ maintained its original nanoparticulate morphology after the OER. The obvious agglomeration was observed in the TEM image [[Figure 5B](#)]. This can be due to the bonding effect of residual Nafion, which came from the electrode preparation process. Moreover, the SAED pattern [inset image in [Figure 5B](#)] of the nanoparticles showed a series of polycrystalline diffraction rings. Compared with the SAED pattern of original IrCoO_x-CO₃²⁻, several new diffraction rings corresponding to other crystal planes were observed after the OER [[Supplementary Figure 21](#)]. The structure was analyzed in more detail using the HRTEM, which also showed the hybrid crystal structures composed of crystalline and amorphous nanoparticles after the OER [[Figure 5C](#)]. As anticipated, a thin CoOOH layer was proved to form on the surface of IrCoO_x-CO₃²⁻, which should be attributed to the high-valence Co⁴⁺^[34,56]. Owing to the instability of high-valence Co⁴⁺ after the decrease in the applied potential, it was transformed into the more stable CoOOH^[51]. There were similar structural transformations on both IrCoO_x-PO₄³⁻ and IrCoO_x-OH⁻ after the OER [[Supplementary Figures 22 and 23](#)]. Moreover, EDS result [[Figure 5D](#)] of IrCoO_x-CO₃²⁻ after the OER revealed a uniform distribution of various elements. However, the mapping of C element indicated a slight decrease in the amount of C element on the surface, which can be attributed to the formation of more high-valence active species, leading to the decomposition of carbonate anions in IrCoO_x-CO₃²⁻. Therefore, the IrCoO_x-CO₃²⁻ with the hybrid crystal structures has excellent structural and compositional stability during the long-term OER process.

CONCLUSIONS

In summary, Ir-doped CoO_x-CO₃²⁻ with hybrid crystalline/amorphous structures was synthesized using an effective coprecipitation approach. The excellent OER activity of IrCoO_x-CO₃²⁻ can be attributed to its adaptable coordination environment and electronic structure, along with the increased interface between the amorphous and crystalline regions. By optimizing Ir content and the types of anions, the optimal IrCoO_x-CO₃²⁻ has delivered 10 mA cm⁻² in 1 M KOH at an extremely low overpotential of 207 mV. *In situ* Raman spectra indicated that Ir doping decreased the potential for forming high-valence Co⁴⁺ in the OER, which explained the high electrocatalytic activity. Moreover, the ultra-long stability of IrCoO_x-CO₃²⁻ in the alkaline media renders it suitable for industrial applications. Thus, the developed Ir-doped Co-based compounds rich in anions are promising candidates for high-performance and low-cost OER electrocatalysts. This study provides a novel approach for the dual regulation of cations and anions in Co-based electrocatalysts, which promote the development of water electrolysis.

DECLARATIONS

Acknowledgments

SEM and EDS were carried out at the Center for Advancing Materials Performance from the Nanoscale (CAMP Nano). We thank Ms. Xiaohua Cheng for her assistance with SEM and EDS measurements.

Author's contributions

Made substantial contributions to design of the study and performed writing: Rong, W.

Assist in processing and analyzing data: Huang, K.; Dong, L.; Xia, J.; Dang, R.

Collected literature and conducted DFT calculations: Chen, Y.

Assist in collecting literature and researching the background: Liu, J.

Made substantial contributions to conception of the study and provided financial support: Cao, Q.; Zhang, B.

Revised the logic and grammar of the article: Wu, J.

Availability of data and materials

The relevant data and materials for the results of this study can be obtained from the first author or corresponding author upon reasonable request.

Financial support and sponsorship

This research was supported by the National Natural Science Foundation of China (Program Nos. 52371051 and 22202158), the Natural Science Foundation of Beijing Municipality (Grant No. 2212037), the Young Talents Program of Shaanxi Province (CLGC202203), and the Research project of Northwest Non-ferrous Metals Research Institute (Program No. YK2321). SEM and EDS measurement was carried out at the Center for Advancing Materials Performance from the Nanoscale (CAMP NANO).

Conflicts of interest

All authors declared that there are no conflicts of interest.

Ethical approval and consent to participate

Not applicable.

Consent for publication

Not applicable.

Copyright

© The Author(s) 2025.

REFERENCES

1. Lagadec, M. F.; Grimaud, A. Water electrolyzers with closed and open electrochemical systems. *Nat. Mater.* **2020**, *19*, 1140-50. [DOI](#) [PubMed](#)
2. Gao, X.; Chen, Y.; Wang, Y.; et al. Next-generation green hydrogen: progress and perspective from electricity, catalyst to electrolyte in electrocatalytic water splitting. *Nanomicro. Lett.* **2024**, *16*, 237. [DOI](#) [PubMed](#) [PMC](#)
3. Qian, Q.; Wang, W.; Wang, G.; et al. Phase-selective synthesis of ruthenium phosphide in hybrid structure enables efficient hybrid water electrolysis under pH-universal conditions. *Small* **2022**, *18*, e2200242. [DOI](#)
4. Wang, X.; Xi, S.; Huang, P.; et al. Pivotal role of reversible NiO₆ geometric conversion in oxygen evolution. *Nature* **2022**, *611*, 702-8. [DOI](#)
5. Hu, C.; Zhang, L.; Gong, J. Recent progress made in the mechanism comprehension and design of electrocatalysts for alkaline water splitting. *Energy. Environ. Sci.* **2019**, *12*, 2620-45. [DOI](#)
6. Fu, X.; Shi, R.; Jiao, S.; Li, M.; Li, Q. Structural design for electrocatalytic water splitting to realize industrial-scale deployment: strategies, advances, and perspectives. *J. Energy. Chem.* **2022**, *70*, 129-53. [DOI](#)
7. Wang, Z.; Xiao, B.; Lin, Z.; et al. In-situ surface decoration of RuO₂ nanoparticles by laser ablation for improved oxygen evolution reaction activity in both acid and alkali solutions. *J. Energy. Chem.* **2021**, *54*, 510-8. [DOI](#)
8. Dang, Q.; Lin, H.; Fan, Z.; et al. Iridium metallene oxide for acidic oxygen evolution catalysis. *Nat. Commun.* **2021**, *12*, 6007. [DOI](#) [PubMed](#) [PMC](#)
9. Wu, Z.; Lu, X. F.; Zang, S.; Lou, X. W. Non-noble-metal-based electrocatalysts toward the oxygen evolution reaction. *Adv. Funct. Mater.* **2020**, *30*, 1910274. [DOI](#)
10. Zhang, Z.; Li, X.; Zhong, C.; et al. Spontaneous synthesis of silver-nanoparticle-decorated transition-metal hydroxides for enhanced

- oxygen evolution reaction. *Angew. Chem. Int. Ed.* **2020**, *59*, 7245-50. DOI
11. Yu, J.; Yu, F.; Yuen, M.; Wang, C. Two-dimensional layered double hydroxides as a platform for electrocatalytic oxygen evolution. *J. Mater. Chem. A* **2021**, *9*, 9389-430. DOI
 12. Zhang, M.; Zhang, Y.; Ye, L.; Guo, B.; Gong, Y. Hierarchically constructed Ag nanowires shelled with ultrathin Co-LDH nanosheets for advanced oxygen evolution reaction. *Appl. Catal. B. Environ.* **2021**, *298*, 120601. DOI
 13. Wang, T.; Liu, X.; Li, Y.; Li, F.; Deng, Z.; Chen, Y. Ultrasonication-assisted and gram-scale synthesis of Co-LDH nanosheet aggregates for oxygen evolution reaction. *Nano. Res.* **2020**, *13*, 79-85. DOI
 14. Zhang, J.; Yan, Y.; Mei, B.; et al. Local spin-state tuning of cobalt-iron selenide nanoframes for the boosted oxygen evolution. *Energy. Environ. Sci.* **2021**, *14*, 365-73. DOI
 15. Li, F.; Ai, H.; Liu, D.; Lo, K. H.; Pan, H. An enhanced oxygen evolution reaction on 2D CoOOH via strain engineering: an insightful view from spin state transition. *J. Mater. Chem. A* **2021**, *9*, 17749-59. DOI
 16. Li, X.; Ge, L.; Du, Y.; et al. Highly oxidized oxide surface toward optimum oxygen evolution reaction by termination engineering. *ACS. Nano* **2023**, *17*, 6811-21. DOI
 17. Hicks, J.; Mansikkamäki, A.; Vasko, P.; Goicoechea, J. M.; Aldridge, S. A nucleophilic gold complex. *Nat. Chem.* **2019**, *11*, 237-41. DOI
 18. Wang, D.; Li, Q.; Han, C.; Lu, Q.; Xing, Z.; Yang, X. Atomic and electronic modulation of self-supported nickel-vanadium layered double hydroxide to accelerate water splitting kinetics. *Nat. Commun.* **2019**, *10*, 3899. DOI PubMed PMC
 19. Xu, H.; Liu, T.; Bai, S.; et al. Cation exchange strategy to single-atom noble-metal doped CuO nanowire arrays with ultralow overpotential for H₂O splitting. *Nano. Lett.* **2020**, *20*, 5482-9. DOI
 20. Cao, D.; Zhang, Z.; Cui, Y.; et al. Frontispiz: one-step approach for constructing high-density single-atom catalysts toward overall water splitting at industrial current densities. *Angew. Chem. Int. Ed.* **2023**, *135*, e202380961. DOI
 21. Liang, X.; Shi, L.; Liu, Y.; et al. Activating inert, nonprecious perovskites with iridium dopants for efficient oxygen evolution reaction under acidic conditions. *Angew. Chem. Int. Ed.* **2019**, *58*, 7631-5. DOI
 22. Wang, Q.; Zhang, Z.; Cai, C.; et al. Single iridium atom doped Ni₃P catalyst for optimal oxygen evolution. *J. Am. Chem. Soc.* **2021**, *143*, 13605-15. DOI
 23. Li, P.; Duan, X.; Kuang, Y.; Sun, X. Iridium in tungsten trioxide matrix as an efficient Bi-functional electrocatalyst for overall water splitting in acidic media. *Small* **2021**, *17*, e2102078. DOI
 24. Wang, P.; Zhang, C.; Ding, J.; Ji, Y.; Li, Y.; Zhang, W. Motivating inert strontium manganate with iridium dopants as efficient electrocatalysts for oxygen evolution in acidic electrolyte. *Small* **2024**, *20*, e2305662. DOI
 25. Liu, J.; Xiao, J.; Wang, Z.; et al. Structural and electronic engineering of Ir-doped Ni-(Oxy)hydroxide nanosheets for enhanced oxygen evolution activity. *ACS. Catal.* **2021**, *11*, 5386-95. DOI
 26. Yin, J.; Jin, J.; Lu, M.; et al. Iridium single atoms coupling with oxygen vacancies boosts oxygen evolution reaction in acid media. *J. Am. Chem. Soc.* **2020**, *142*, 18378-86. DOI
 27. Zhao, W.; Xu, F.; Liu, L.; Liu, M.; Weng, B. Strain-induced electronic structure modulation on MnO₂ nanosheet by Ir incorporation for efficient water oxidation in acid. *Adv. Mater.* **2023**, *35*, e2308060. DOI
 28. You, H.; Wu, D.; Si, D.; et al. Monolayer NiIr-layered double hydroxide as a long-lived efficient oxygen evolution catalyst for seawater splitting. *J. Am. Chem. Soc.* **2022**, *144*, 9254-63. DOI
 29. Wang, X.; Ma, R.; Li, S.; et al. In situ electrochemical oxanion steering of water oxidation electrocatalysts for optimized activity and stability. *Adv. Energy. Mater.* **2023**, *13*, 2300765. DOI
 30. Liang, R.; Zhang, B.; Du, Y.; Han, X.; Li, S.; Xu, P. Understanding the anion effect of basic cobalt salts for the electrocatalytic oxygen evolution reaction. *ACS. Catal.* **2023**, *13*, 8821-9. DOI
 31. Wang, A.; Wang, W.; Xu, J.; et al. Enhancing oxygen evolution reaction by simultaneously triggering metal and lattice oxygen redox pair in iridium loading on Ni-doped Co₃O₄. *Adv. Energy. Mater.* **2023**, *13*, 2302537. DOI
 32. Cao, J.; Mou, T.; Mei, B.; et al. Improved electrocatalytic activity and stability by single iridium atoms on iron-based layered double hydroxides for oxygen evolution. *Angew. Chem. Int. Ed.* **2023**, *135*, e202310973. DOI
 33. Zhu, Y.; Wang, J.; Koketsu, T.; et al. Iridium single atoms incorporated in Co₃O₄ efficiently catalyze the oxygen evolution in acidic conditions. *Nat. Commun.* **2022**, *13*, 7754. DOI PubMed PMC
 34. Chen, M.; Liu, D.; Feng, J.; et al. In-situ generation of Ni-CoOOH through deep reconstruction for durable alkaline water electrolysis. *Chem. Eng. J.* **2022**, *443*, 136432. DOI
 35. Li, X.; Zhang, H.; Hu, Q.; et al. Amorphous NiFe oxide-based nanoreactors for efficient electrocatalytic water oxidation. *Angew. Chem. Int. Ed.* **2023**, *62*, e202300478. DOI
 36. Guan, D.; Zhou, W.; Shao, Z. Rational design of superior electrocatalysts for water oxidation: crystalline or amorphous structure? *Small. Sci.* **2021**, *1*, 2100030. DOI
 37. Hu, Y.; Luo, G.; Wang, L.; et al. Single Ru atoms stabilized by hybrid amorphous/crystalline FeCoNi layered double hydroxide for ultraefficient oxygen evolution. *Adv. Energy. Mater.* **2021**, *11*, 2002816. DOI
 38. Wu, J.; Yang, T.; Fu, R.; et al. Constructing electrocatalysts with composition gradient distribution by solubility product theory: amorphous/crystalline CoNiFe-LDH hollow nanocages. *Adv. Funct. Mater.* **2023**, *33*, 2300808. DOI
 39. Li, D.; Qin, Y.; Liu, J.; et al. Dense crystalline-amorphous interfacial sites for enhanced electrocatalytic oxygen evolution. *Adv. Funct. Mater.* **2022**, *32*, 2107056. DOI

40. Jiang, C.; Yang, J.; Han, X.; et al. Crystallinity-modulated $\text{Co}_{2-x}\text{V}_x\text{O}_4$ nanoplates for efficient electrochemical water oxidation. *ACS Catal.* **2021**, *11*, 14884-91. DOI
41. Li, Z.; Zhang, X.; Kang, Y.; et al. Interface engineering of Co-LDH@MOF heterojunction in highly stable and efficient oxygen evolution reaction. *Adv. Sci.* **2021**, *8*, 2002631. DOI PubMed PMC
42. Dai, S.; Zhang, Z.; Xu, J.; et al. In situ Raman study of nickel bicarbonate for high-performance energy storage device. *Nano. Energy.* **2019**, *64*, 103919. DOI
43. Begildayeva, T.; Theerthagiri, J.; Lee, S. J.; Yu, Y.; Choi, M. Y. Unraveling the synergy of anion modulation on Co electrocatalysts by pulsed laser for water splitting: intermediate capturing by in situ/operando Raman studies. *Small* **2022**, *18*, e2204309. DOI
44. Sui, P.; Gao, M.; Liu, S.; Xu, C.; Zhu, M.; Luo, J. Carbon dioxide valorization via Formate electrosynthesis in a wide potential window. *Adv. Funct. Mater.* **2022**, *32*, 2203794. DOI
45. He, Y.; Zhou, W.; Li, D.; et al. Rare earth doping engineering tailoring advanced oxygen-vacancy Co_3O_4 with tunable structures for high-efficiency energy storage. *Small* **2023**, *19*, e2206956. DOI
46. Qi, J.; Lin, Y.; Chen, D.; Zhou, T.; Zhang, W.; Cao, R. Autologous cobalt phosphates with modulated coordination sites for electrocatalytic water oxidation. *Angew. Chem. Int. Ed.* **2020**, *132*, 9002-6. DOI
47. Wang, C.; Zhai, P.; Xia, M.; et al. Engineering lattice oxygen activation of iridium clusters stabilized on amorphous bimetal borides array for oxygen evolution reaction. *Angew. Chem. Int. Ed.* **2021**, *133*, 27332-40. DOI
48. Zhang, N.; Feng, X.; Rao, D.; et al. Lattice oxygen activation enabled by high-valence metal sites for enhanced water oxidation. *Nat. Commun.* **2020**, *11*, 4066. DOI PubMed PMC
49. Huang, H.; Ning, S.; Xie, Y.; et al. Synergistic modulation of electronic interaction to enhance intrinsic activity and conductivity of Fe-Co-Ni hydroxide nanotube for highly efficient oxygen evolution electrocatalyst. *Small* **2023**, *19*, e2302272. DOI
50. Feng, C.; Zhang, Z.; Wang, D.; et al. Tuning the electronic and steric interaction at the atomic interface for enhanced oxygen evolution. *J. Am. Chem. Soc.* **2022**, *144*, 9271-9. DOI
51. Yao, N.; Wang, G.; Jia, H.; et al. Intermolecular energy gap-induced formation of high-valent cobalt species in CoOOH surface layer on cobalt sulfides for efficient water oxidation. *Angew. Chem. Int. Ed.* **2022**, *134*, e202117178. DOI
52. Gao, P.; Zeng, Y.; Tang, P.; et al. Understanding the synergistic effects and structural evolution of $\text{Co}(\text{OH})_2$ and Co_3O_4 toward boosting electrochemical charge storage. *Adv. Funct. Mater.* **2022**, *32*, 2108644. DOI
53. Zhu, W.; Yao, F.; Cheng, K.; et al. Direct dioxygen radical coupling driven by octahedral ruthenium-oxygen-cobalt collaborative coordination for acidic oxygen evolution reaction. *J. Am. Chem. Soc.* **2023**, *145*, 17995-8006. DOI
54. Tang, K.; Hu, H.; Xiong, Y.; et al. Hydrophobization engineering of the air-cathode catalyst for improved oxygen diffusion towards efficient zinc-air batteries. *Angew. Chem. Int. Ed.* **2022**, *61*, e202202671. DOI
55. Zhang, B.; Wang, L.; Cao, Z.; et al. High-valence metals improve oxygen evolution reaction performance by modulating 3d metal oxidation cycle energetics. *Nat. Catal.* **2020**, *3*, 985-92. DOI
56. Wang, Q.; Li, J.; Li, Y.; Shao, G.; Jia, Z.; Shen, B. Non-noble metal-based amorphous high-entropy oxides as efficient and reliable electrocatalysts for oxygen evolution reaction. *Nano. Res.* **2022**, *15*, 8751-9. DOI